Supplementary Information for: Why increased extreme precipitation under climate change negatively affects water security

Joris P.C. Eekhout[1], Johannes E. Hunink[2], Wilco Terink[3], and Joris de Vente[1]

[1]Soil Erosion and Conservation Research Group, CEBAS-CSIC, Spanish Research Council, Campus Universitario Espinardo, 30100, P.O. Box 164, Murcia, Spain
[2]FutureWater, Calle San Diego 17 4a, 30202, Cartagena, Spain
[3]FutureWater, Costerweg 1V, 6702 AA, Wageningen, The Netherlands

Correspondence: Joris Eekhout (joriseekhout@gmail.com)

1 Model Description

We applied the Spatial Processes in HYdrology (SPHY) hydrological model (Terink et al., 2015), which is a spatially distributed leaky-bucket type of model applied on a cell-by-cell basis at a daily time step. The SPHY model is fully coupled with the Morgan-Morgan-Finney soil erosion model (MMF; Morgan and Duzant, 2008). The SPHY-MMF model is described in detail in Eekhout et al. (2018) and can be accessed at this location: https://github.com/JorisEekhout/SPHY/tree/SPHY2.1-MMF.

1.1 Hydrological Model

SPHY simulates most relevant hydrological processes, such as interception, evapotranspiration, dynamic evolution of vegetation cover (including seasonal patterns and response to climate change), surface runoff, and lateral and vertical soil moisture flow. Here we describe the main modification we made for this study, i.e. the inclusion of a infiltration excess surface runoff equation. See Terink et al. (2015) for a detailed description of the model.

We incorporated an infiltration excess equation, which runs at a daily time step. The equation is inspired by the Green-Ampt formula (Heber Green and Ampt, 1911). We assumed a constant infiltration rate f $(\mathrm{mm\,hr^{-1}})$, which is determined for each cell and each day by:

$$f = \frac{K_{\mathrm{eff}}}{24}\left[1+\frac{\theta_{\mathrm{sat}}-\theta}{\theta_{\mathrm{sat}}}\right]^{\lambda} \tag{1}$$

where K_{eff} is the effective hydraulic conductivity, θ_{sat} is the saturated water content, θ is the actual water content, and λ is a calibration parameter. Bouwer (1969) suggested an approximation of $K_{\mathrm{eff}} \approx 0.5\,K_{\mathrm{sat}}$.

Infiltration excess surface runoff occurs when the precipitation intensity exceeds the infiltration rate f (Beven, 2012). Analysis of hourly precipitation time series for 25 years (1991-2015) from 5 precipitation stations in the catchment showed that, on average, the highest precipitation intensity was recorded in the first hour of the rain storm and decreases linearly until the end of the storm. We assumed a triangular-shaped precipitation intensity $p(t)$ $(\mathrm{mm\,hr^{-1}})$ according to:

$$p(t) = -\frac{1}{2}\alpha^2 Pt + \alpha P \tag{2}$$

where α is the fraction of daily rainfall that occurs in the hour with the highest intensity, P is the daily rainfall (mm), and t is an hourly time step. Daily infiltration excess surface runoff Q_{surf} is determined as follows:

$$Q_{\mathrm{surf}} = \begin{cases} \dfrac{(\alpha P - f)^2}{\alpha^2 P} & \text{if } \alpha P > f \\ 0 & \text{if } \alpha P \leq f \end{cases} \tag{3}$$

When the hourly precipitation intensity αP is higher than the infiltration rate f, surface runoff equals the triangular shaped area of the precipitation above the infiltration rate. The amount of precipitation below the infiltration rate will infiltrate into the rootzone. Parameter α was set to 0.34, which follows from the analysis of the hourly rainfall data.

1.2 Daily Morgan-Morgan-Finney soil erosion model

We integrated the Morgan-Morgan-Finney (MMF; Morgan and Duzant, 2008) soil erosion model into the SPHY hydrological model. MMF is a conceptual soil erosion model that originally is applied at an annual time step. We modified the original MMF model such that it runs at a daily time step and is fully integrated into the SPHY model. This means that MMF receives input from the SPHY model, such as effective precipitation (throughfall), runoff and canopy cover.

Detachment of soil particles is determined separately for raindrop impact and surface runoff. The detachment of soil particles by raindrop impact (F; $\mathrm{kg\,m^{-2}}$) is a function of the kinetic energy of the effective rainfall, the detachability of the soil (K; $\mathrm{J\,m^{-2}}$) and the ground cover (GC; expressed as a proportion between zero and unity). The kinetic energy of the effective rainfall is in turn determined separately for direct throughfall and leaf drainage, and is subsequently summed to obtain the total rainfall energy KE. Canopy cover (fraction between 0 and 1 and obtained from the dynamic vegetation module) is used to separate direct throughfall and leaf drop from effective precipitation. The ground cover protects the soil from detachment and includes the proportion of vegetation and stones covering the surface and is set to 1 in case of the presence of snow. In order to allow for the particle-size distribution of the soil, the effective rainfall is proportioned according to the proportion of clay (c), silt (z) and sand (s) particles in the soil and subsequently summed:

$$F = K_i \frac{\%i}{100}(1 - GC)KE \times 10^{-3} \tag{4}$$

With i the textural class, with c for clay, z for silt and s for sand. Based on data from Quansah (1982), values of K_c, K_z and K_s are taken respectively as 0.1, 0.5 and 0.3 $\mathrm{g\,J^{-1}}$.

The detachment of soil particles by runoff (H; $\mathrm{kg\,m^{-2}}$) is a function of the volume of accumulated runoff (Q; mm), the detachability of the soil by runoff (DR; $\mathrm{g\,mm^{-1}}$), the slope angle (S; °) and the ground cover (GC; -). The detachment by runoff is also proportioned by texture class and subsequently summed:

$$H = DR_i \frac{\%i}{100} Q^{1.5}(1 - GC)\sin^{0.3} S \times 10^{-3} \tag{5}$$

Based on data from Quansah (1982), values of DR_c, DR_z and DR_s are taken respectively as 1.0, 1.6 and 1.5 $\mathrm{g\,mm^{-1}}$.

The detachment of soil particles by raindrop impact (F) and runoff (H) are subsequently summed. Only a proportion of the detached soil will be delivered to the runoff for transport, the remainder will be deposited within the cell of its origin. The percentage of the detached sediment that is deposited within the cell of its origin is estimated from the relationship obtained by Tollner et al. (1976), calculated separately for each particle size:

$$DEP_{c,z,s} = 44.1 N_{f_{c,z,s}}^{0.29} \tag{6}$$

Where N_f is the particle fall number and DEP is maximized by 100. The particle fall number is a function of the flow velocity, which is a function of the presence and abundance of vegetation and the surface roughness.

The amount of soil particles that will be delivered to the runoff for transport is calculated as follows:

$$G = \sum_{c,z,s} (F_{c,z,s} + H_{c,z,s})(1 - (DEP_{c,z,s}/100)) \tag{7}$$

1.3 Sediment Routing

Transport of sediment by runoff is restricted by the transport capacity of the flow. We modified the transport capacity equation as proposed by Prosser and Rustomji (2000) by introducing a landuse-specific roughness factor:

$$TC = \text{flow}_{\text{factor}} q^{\beta}\ S^{\gamma} \tag{8}$$

Where $\text{flow}_{\text{factor}}$ is a spatially distributed roughness factor, q is the accumulated runoff per unit width ($\mathrm{m}^2\ \mathrm{day}^{-1}$), S is the local energy gradient, approximated by the slope, and β and γ are model parameters. As suggested by Prosser and Rustomji (2000) we set $\gamma = 1.4$ and we used β in the calibration procedure. The landuse-specific roughness factor $\text{flow}_{\text{factor}}$ is a function of the presence and abundance of vegetation and the surface roughness.

Reservoir sediment trapping efficiency, the percentage of sediment trapped by the reservoir, is calculated according to Brown (1943):

$$TE = 100 \left[1 - \frac{1}{1 + 0.0021 D \frac{C}{A_{\text{basin}}}} \right] \tag{9}$$

where TE is the trapping efficiency (%), D is a constant within the range 0.046-1, we adopted the mean value of 0.1, C is the reservoir capacity (m^3), and A_{basin} is the drainage area of the subcatchment (km^2).

1.4 Dynamic Vegetation Module

SPHY-MMF includes a dynamic vegetation module that allows characterization of the seasonal and inter-annual differences in vegetation cover. A time series of the Normalized Difference Vegetation Index (NDVI) images is used as input for the dynamic vegetation module. The Leaf Area Index (LAI) is determined from the individual NDVI images using a logarithmic relation (Sellers et al., 1996). The LAI is used in the hydrological model to determine canopy storage, interception and the resulting precipitation throughfall. The latter is subsequently used in both the hydrological and soil erosion model. The canopy cover, from the soil erosion model, is defined as the LAI maximized by 1. The NDVI is also used to determine the crop coefficients, which are used in the calculation of the potential evapotranspiration. Crop coefficients are determined from NDVI with a linear relation. See Terink et al. (2015) for a detailed description of the dynamic vegetation module.

1.5 Model input data

All model input data were prepared at a 200 m resolution. Textural fractions (sand, clay and silt) and organic matter content were obtained from the global SoilGrids dataset (Hengl et al., 2017) at 250 m resolution. The soil hydraulic properties (saturated hydraulic conductivity, saturated water content, field capacity, and wilting point) were obtained by applying pedotransfer functions (Saxton and Rawls, 2006).

The SRTM dataset (Farr et al., 2007) at 30 m resolution was resampled to the model grid to obtain a Digital Elevation Model (Figure 1d). The spatially distributed rock fraction map was obtained by applying the empirical formulations from Poesen et al. (1998), which determines rock fraction based on slope.

Both the hydrological and the soil erosion model require landuse-specific input. We used a national landuse map (Ministerio de Agricultura y Pesca Alimentación y Medio Ambiente, 2010), which provides 57 landuse classes within the study area. Values for the landuse-specific tabular value of the depletion fraction were obtained from Allen et al. (1998) (Table 22). Values for the maximum LAI were obtained from Sellers et al. (1996). The soil erosion model requires landuse-specific input for plant height, stem density, stem diameter, canopy cover fraction, ground cover fraction and Manning's roughness coefficient for vegetation. We obtained values for each of these parameters through observations from aerial photographs, expert judgement and as part of the calibration procedure.

NDVI images were obtained from bi-monthly Moderate Resolution Imaging Spectroradiometer (MODIS) data for the period 2000-2012. For model calibration (2001-2010) we used each of the individual NDVI images, after gap-filling (mainly due to cloud cover) with the long-term average 16-day period NDVI for the period 2000-2012.

For the reference and future scenarios no NDVI images of sufficient quality and resolution were available, therefore we prepared the NDVI model input, accounting for the intra- and inter-annual variability. The intra-annual variability was obtained from the long-term average 16-day period NDVI for the period 2000-2012. The inter-annual variability was determined based on a log-linear relationship between the annual precipitation sum, annual average temperature, annual maximum temperature and annual average NDVI for each of the 57 landuse classes for the period 2000-2012:

$$\begin{aligned} NDVI_{\text{year}} =& \beta_0 + \log(P_{\text{year}})\beta_1 + \log(P_{\text{year-1}})\beta_2 + \log(Tavg_{\text{year}})\beta_3 \\ &+ \log(Tavg_{\text{year-1}})\beta_4 + \log(Tmax_{\text{year}})\beta_5 + \log(Tmax_{\text{year-1}})\beta_6 \end{aligned} \tag{10}$$

Where $NDVI$ is the annual average NDVI, P the annual precipitation sum, $Tavg$ the annual average temperature, $Tmax$ the annual maximum temperature, and β_{0-6} coefficients of the log-linear regression model. We used the annual climate indices of two years, the current year and the previous year, to account for the climate lag that may influence the vegetation development. A stepwise model selection procedure was applied for each of the 57 landuse classes, selecting the best combination of variables from equation 10 with the lowest AIC (Akaike Information Criterion) in R (version 3.4.0), using the stepAIC algorithm from the MASS package (Venables and Ripley, 2002).

1.6 Model Calibration & Validation

Model calibration and validation were performed in five headwater subcatchments that are not affected by water extractions for irrigation (Figure 1b). Calibration and validation were performed for the periods 2001-2010 and 1987-2000, respectively.

Daily discharge time series were used to determine model performance. Data were obtained from the Segura River Basin Agency for the Fuensanta reservoir (Figure 1b). We only considered the discharge originating from the Fuensanta subcatchment, by subtracting the discharge from the upstream located subcatchments, both for the observed and the simulated time series. The calibration procedure consisted of two steps. First, we optimized the water balance by comparing the observed and simulated discharge sum (percent bias). We adjusted the calibration parameter λ from equation 3 and model parameters from the dynamic vegetation module and soil hydraulic properties to optimize the percent bias of the discharge. In the second step we optimized the Nash-Sutcliffe model efficiency (NSE; Nash and Sutcliffe, 1970)) by adjusting a model parameter from the routing module. The calibration resulted in a NSE of 0.47 for the daily discharge, a NSE of 0.76 for the monthly discharge and a percent bias of 2.3% (Figure S1a). Model validation resulted in a NSE of 0.25 for the daily discharge, a NSE of 0.39 for the monthly discharge and a percent bias of -18.7% (Figure S1b).

Next, we calibrated the soil erosion model. First, we optimized the detached material going into transport G for 8 aggregated landuse classes, based on literature data (Cerdan et al., 2010; Maetens et al., 2012). We optimized sediment yield at the reservoirs with reservoir sediment yield data from 4 reservoirs (Avendaño-Salas et al., 1997) (Figure 1b). Model performance was evaluated based on percent bias. The calibration procedure focused on a model parameter from the sediment transport module. We obtained a percent bias of 0.0% in the calibration and -19.8% in the validation.

2 Global Infiltration Excess Surface Runoff

Infiltration excess surface runoff occurs when the precipitation intensity exceeds the soil infiltration rate (Beven, 2012). Based on global precipitation and soil data, we determined a global map indicating the areas prone for infiltration excess runoff during extreme precipitation events.

Global daily precipitation data were obtained from the Global Precipitation Climatology Centre (GPCC; Schamm et al., 2016). The GPCC dataset contains daily global land-surface precipitation data, interpolated on a regular 1° grid for the period 1988-2013. For each grid cell we determined the extreme precipitation (Figure S2a), defined as the 95th percentile of daily precipitation, considering only rainy days ($>1\ \mathrm{mm\,day^{-1}}$, Jacob et al., 2014). Infiltration excess runoff is a sub-daily process. While no global sub-daily precipitation data were available, we assumed that 34% of the daily rainfall occurs in the hour with the highest intensity. This fraction we obtained from analysis of hourly precipitation data from 5 precipitation stations within the Segura River catchment covering a period of 25 years (1991-2015). While this fraction may vary globally, in the absence of better estimates we extrapolated the fraction to illustrate the potential extent of global sensitive areas to infiltration excess runoff.

Infiltration rate was estimated based on the saturated hydraulic conductivity. We obtained global sand, clay and organic matter maps at 10 km resolution from the SoilGrids dataset (Hengl et al., 2017). Saturated hydraulic conductivity (Figure S2b) was obtained by applying pedotransfer functions (Saxton and Rawls, 2006). To obtain an estimate of the infiltration rate we determined the effective saturated hydraulic conductivity K_{eff}. Bouwer (1969) showed that, because of entrapped air, K_{eff} should be smaller than K_{sat} and suggested an approximation of $K_{\mathrm{eff}} \approx 0.5\, K_{\mathrm{sat}}$.

References

Allen, R. G., Pereira, L., Raes, D., and Smith, M.: Crop evapotranspiration: Guidelines for computing crop requirements, Tech. Rep. 56, https://doi.org/10.1016/j.eja.2010.12.001, http://www.kimberly.uidaho.edu/water/fao56/fao56.pdf, 1998.

Avendaño-Salas, C., Sanz-Montero, E., Cobo-Rayán, R., and Gómez-Montaña, J. L.: Capacity Situation in Spanish Reservoirs, in: ICOLD, Proceedings of the 19th International Symposium on Large Dams, pp. 849–862, Florence, 1997.

Beven, K. J.: Rainfall-runoff modelling: the primer, John Wiley & Sons, Ltd, https://doi.org/10.1002/9781119951001, http://www.scopus.com/inward/record.url?eid=2-s2.0-84888749158{&}partnerID=tZOtx3y1, 2012.

Bouwer, H.: Infiltration of Water into Nonuniform Soil, Journal of the Irrigation and Drainage Division, 95, 451–462, 1969.

Brown, C. B.: Discussion of Sedimentation in reservoirs, in: Transactions of the American Society of Civil Engineers 69, pp. 1493–1500, 1943.

Cerdan, O., Govers, G., Le Bissonnais, Y., Van Oost, K., Poesen, J., Saby, N., Gobin, A., Vacca, A., Quinton, J., Auerswald, K., Klik, A., Kwaad, F. J. P. M., Raclot, D., Ionita, I., Rejman, J., Rousseva, S., Muxart, T., Roxo, M. J., and Dostal, T.: Rates and spatial variations of soil erosion in Europe: A study based on erosion plot data, Geomorphology, 122, 167–177, https://doi.org/10.1016/j.geomorph.2010.06.011, http://dx.doi.org/10.1016/j.geomorph.2010.06.011, 2010.

Eekhout, J. P. C., Terink, W., and de Vente, J.: Assessing the large-scale impacts of environmental change using a coupled hydrology and soil erosion model, Earth Surface Dynamics Discussions, pp. 1–27, https://doi.org/10.5194/esurf-2018-25, https://www.earth-surf-dynam-discuss.net/esurf-2018-25/, 2018.

Farr, T. G., Rosen, P. A., Caro, E., Crippen, R., Duren, R., Hensley, S., Kobrick, M., Paller, M., Rodriguez, E., Roth, L., Seal, D., Shaffer, S., Shimada, J., Umland, J., Werner, M., Oskin, M., Burbank, D., and Alsdorf, D.: The Shuttle Radar Topography Mission, Reviews of Geophysics, 45, RG2004, https://doi.org/10.1029/2005RG000183, http://doi.wiley.com/10.1029/2005RG000183, 2007.

Heber Green, W. and Ampt, G. A.: Studies on Soil Phyics., The Journal of Agricultural Science, 4, 1, https://doi.org/10.1017/S0021859600001441, http://www.journals.cambridge.org/abstract{_}S0021859600001441, 1911.

Hengl, T., Mendes de Jesus, J., Heuvelink, G. B. M., Ruiperez Gonzalez, M., Kilibarda, M., Blagotić, A., Shangguan, W., Wright, M. N., Geng, X., Bauer-Marschallinger, B., Guevara, M. A., Vargas, R., MacMillan, R. A., Batjes, N. H., Leenaars, J. G. B., Ribeiro, E., Wheeler, I., Mantel, S., and Kempen, B.: SoilGrids250m: Global gridded soil information based on machine learning, PLOS ONE, 12, e0169 748, https://doi.org/10.1371/journal.pone.0169748, http://dx.plos.org/10.1371/journal.pone.0169748, 2017.

Jacob, D., Petersen, J., Eggert, B., Alias, A., Christensen, O. B., Bouwer, L. M., Braun, A., Colette, A., Déqué, M., Georgievski, G., Georgopoulou, E., Gobiet, A., Menut, L., Nikulin, G., Haensler, A., Hempelmann, N., Jones, C., Keuler, K., Kovats, S., Kröner, N., Kotlarski, S., Kriegsmann, A., Martin, E., van Meijgaard, E., Moseley, C., Pfeifer, S., Preuschmann, S., Radermacher, C., Radtke, K., Rechid, D., Rounsevell, M., Samuelsson, P., Somot, S., Soussana, J.-F., Teichmann, C., Valentini, R., Vautard, R., Weber, B., and Yiou, P.: EURO-CORDEX: new high-resolution climate change projections for European impact research, Regional Environmental Change, 14, 563–578, https://doi.org/10.1007/s10113-013-0499-2, http://link.springer.com/10.1007/s10113-013-0499-2http://download.springer.com/static/pdf/221/art:10.1007/s10113-013-0499-2.pdf?originUrl=http://link.springer.com/article/10.1007/s10113-013-0499-2{&}token2=exp=1462793760{~}acl=/static/pdf/221/art:10.1007/s10, 2014.

Maetens, W., Vanmaercke, M., Poesen, J., Jankauskas, B., Jankauskiene, G., and Ionita, I.: Effects of land use on annual runoff and soil loss in Europe and the Mediterranean: A meta-analysis of plot data, Progress in Physical Geography, 36, 599–653, https://doi.org/10.1177/0309133312451303, http://ppg.sagepub.com/cgi/doi/10.1177/0309133312451303, 2012.

Ministerio de Agricultura y Pesca Alimentación y Medio Ambiente: Mapa de Cultivos y Aprovechamientos de España 2000-2010 (1: 50.000), http://www.magrama.gob.es/es/cartografia-y-sig/publicaciones/agricultura/mac{_}2000{_}2009.aspx, 2010.

Morgan, R. P. C. and Duzant, J. H.: Modified MMF (Morgan–Morgan–Finney) model for evaluating effects of crops and vegetation cover on soil erosion, Earth Surface Processes and Landforms, 33, 90–106, https://doi.org/10.1002/esp.1530, http://doi.wiley.com/10.1002/esp.1530, 2008.

Nash, J. E. and Sutcliffe, J. V.: River Flow Forecasting Through Conceptual Models Part I-a Discussion of Principles*, Journal of Hydrology, 10, 282–290, https://doi.org/10.1016/0022-1694(70)90255-6, 1970.

Poesen, J. W., van Wesemael, B., Bunte, K., and Benet, A. S.: Variation of rock fragment cover and size along semiarid hillslopes: a case-study from southeast Spain, Geomorphology, 23, 323–335, https://doi.org/10.1016/S0169-555X(98)00013-0, http://linkinghub.elsevier.com/retrieve/pii/S0169555X98000130, 1998.

Prosser, I. P. and Rustomji, P.: Sediment transport capacity relations for overland flow, Progress in Physical Geography, 24, 179–193, https://doi.org/10.1177/030913330002400202, http://ppg.sagepub.com/content/24/2/179.full.pdfhttp://ppg.sagepub.com/cgi/doi/10.1177/030913330002400202, 2000.

Quansah, C.: Laboratory experimentation for the statistical derivation of equations for soil erosion modelling and soil conservation design, Ph.D. thesis, http://ethos.bl.uk/OrderDetails.do?uin=uk.bl.ethos.337734, 1982.

Saxton, K. E. and Rawls, W. J.: Soil Water Characteristic Estimates by Texture and Organic Matter for Hydrologic Solutions, Soil Science Society of America Journal, 70, 1569, https://doi.org/10.2136/sssaj2005.0117, https://www.soils.org/publications/sssaj/abstracts/70/5/1569, 2006.

Schamm, K., Ziese, M., Raykova, K., Becker, A., Finger, P., Meyer-Christoffer, A., and Schneider, U.: GPCC Full Data Daily Version 1.0: Daily Land-Surface Precipitation from Rain Gauges built on GTS based and Historic Data, https://doi.org/10.5065/D6V69GRT, https://doi.org/10.5065/D6V69GRT, 2016.

Sellers, P. J., Tucker, C. J., Collatz, G. J., Los, S. O., Justice, C. O., Dazlich, D. A., and Randall, D. A.: A Revised Land Surface Parameterization (SiB2) for Atmospheric GCMS. Part II: The Generation of Global Fields of Terrestrial Biophysical Parameters from Satellite Data, Journal of Climate, 9, 706–737, https://doi.org/10.1175/1520-0442(1996)009<0706:ARLSPF>2.0.CO;2, http://journals.ametsoc.org/doi/abs/10.1175/1520-0442(1996)009{%}3C0706:ARLSPF{%}3E2.0.CO;2, 1996.

Terink, W., Lutz, A. F., Simons, G. W. H., Immerzeel, W. W., and Droogers, P.: SPHY v2.0: Spatial Processes in HYdrology, Geoscientific Model Development, 8, 2009–2034, https://doi.org/10.5194/gmd-8-2009-2015, http://www.geosci-model-dev.net/8/2009/2015/, 2015.

Tollner, E. W., Barfield, B. J., Haan, C. T., and Kao, T. Y.: Suspended Sediment Filtration Capacity of Simulated Vegetation, Transactions of the ASAE, 19, 0678–0682, https://doi.org/10.13031/2013.36095, http://elibrary.asabe.org/abstract.asp??JID=3{&}AID=36095{&}CID=t1976{&}v=19{&}i=4{&}T=1, 1976.

Venables, W. N. and Ripley, B. D.: Modern Applied Statistics with S, Springer, New York, fourth edi edn., 2002.

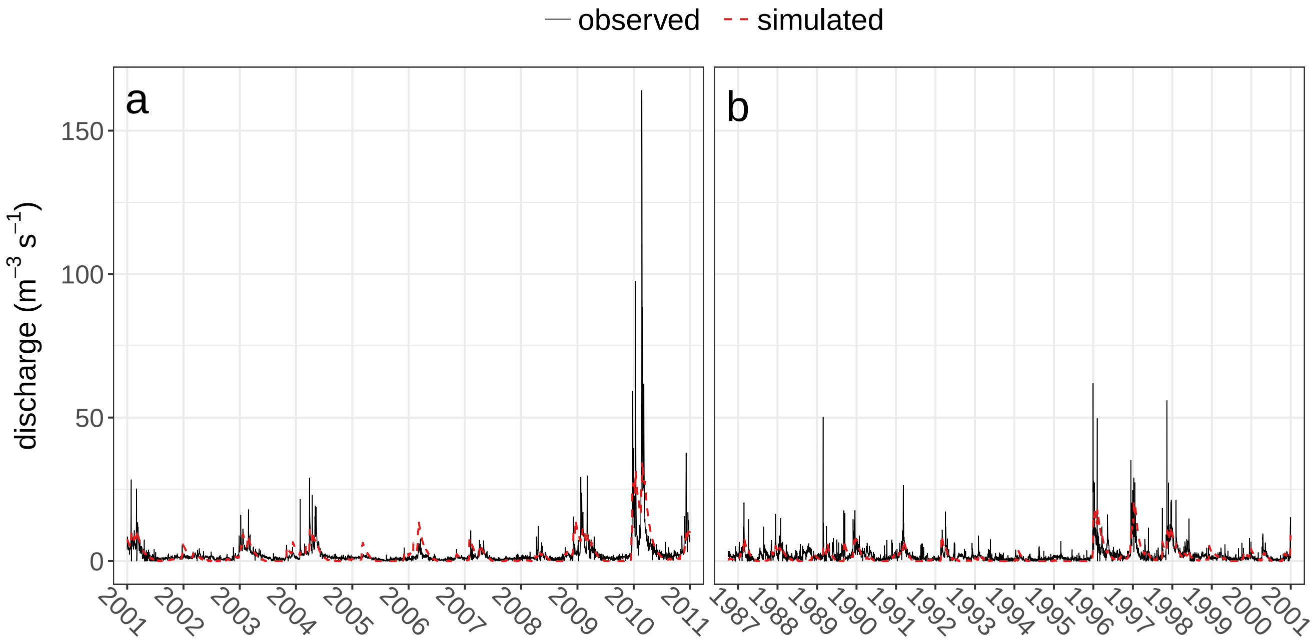

Figure S1. Discharge time series for the calibration (a) and validation period (b). The dashed red line correspond to the simulated time series and the solid black line corresponds to the observed time series.

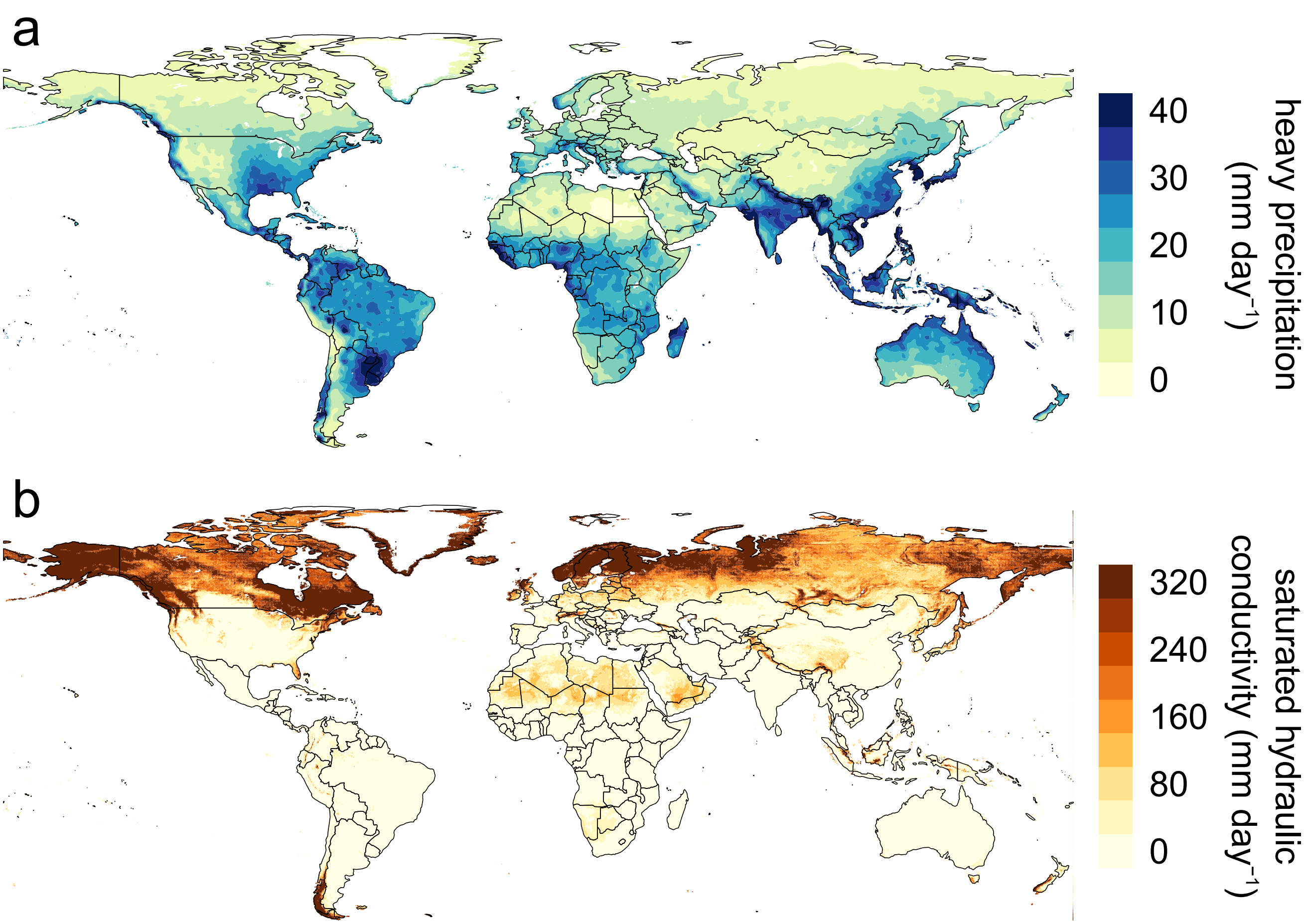

Figure S2. (a) Global heavy precipitation ($\mathrm{mm\,day^{-1}}$) and (b) global saturated hydraulic conductivity map ($\mathrm{mm\,day^{-1}}$).

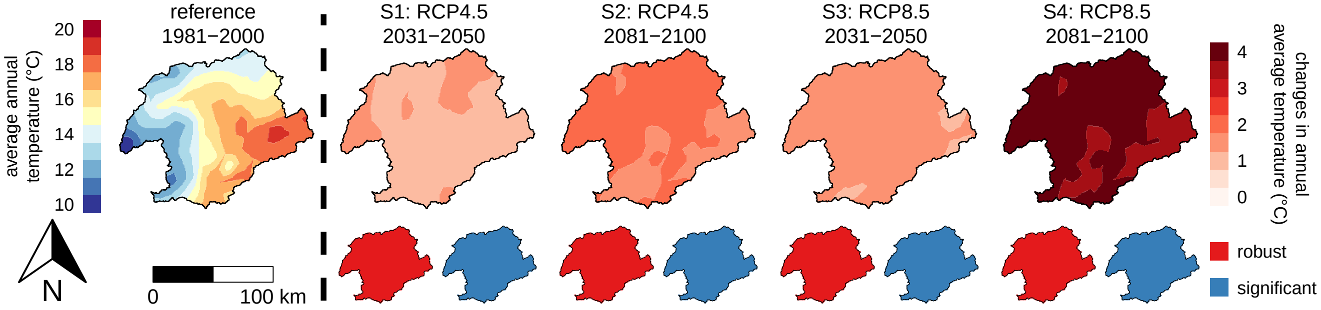

Figure S3. Ensemble average annual-average temperature (°C) for the reference scenario (left) and changes between the reference scenario and the four future scenarios (right).

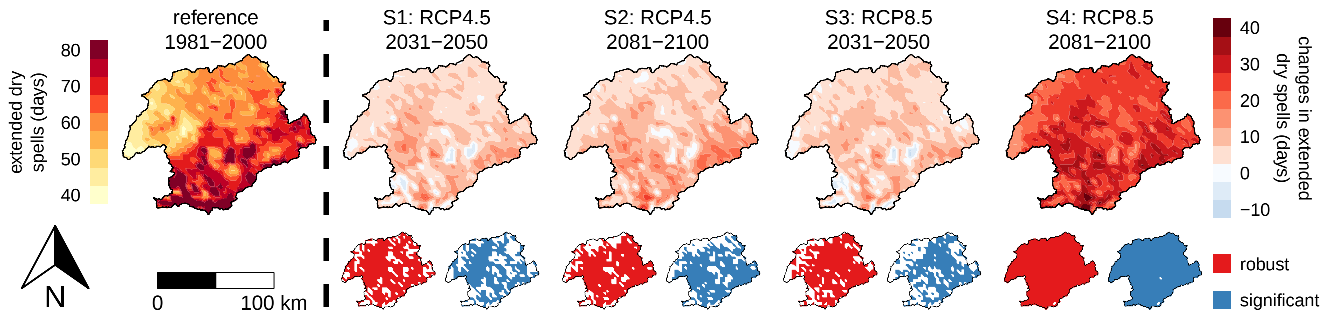

Figure S4. Ensemble average dry spells (days) defined as the 95th percentile of the duration of dry spells, which is defined as periods of at least 5 consecutive days with daily precipitation below 1 mm, for the reference scenario (left) and changes between the reference scenario and the four future scenarios (right).

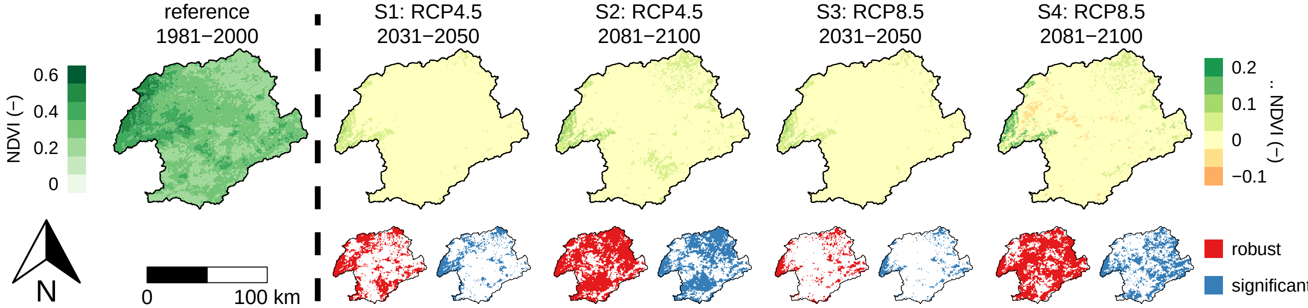

Figure S5. Ensemble average NDVI (-) for the reference scenario (left) and changes between the reference scenario and the four future scenarios (right).

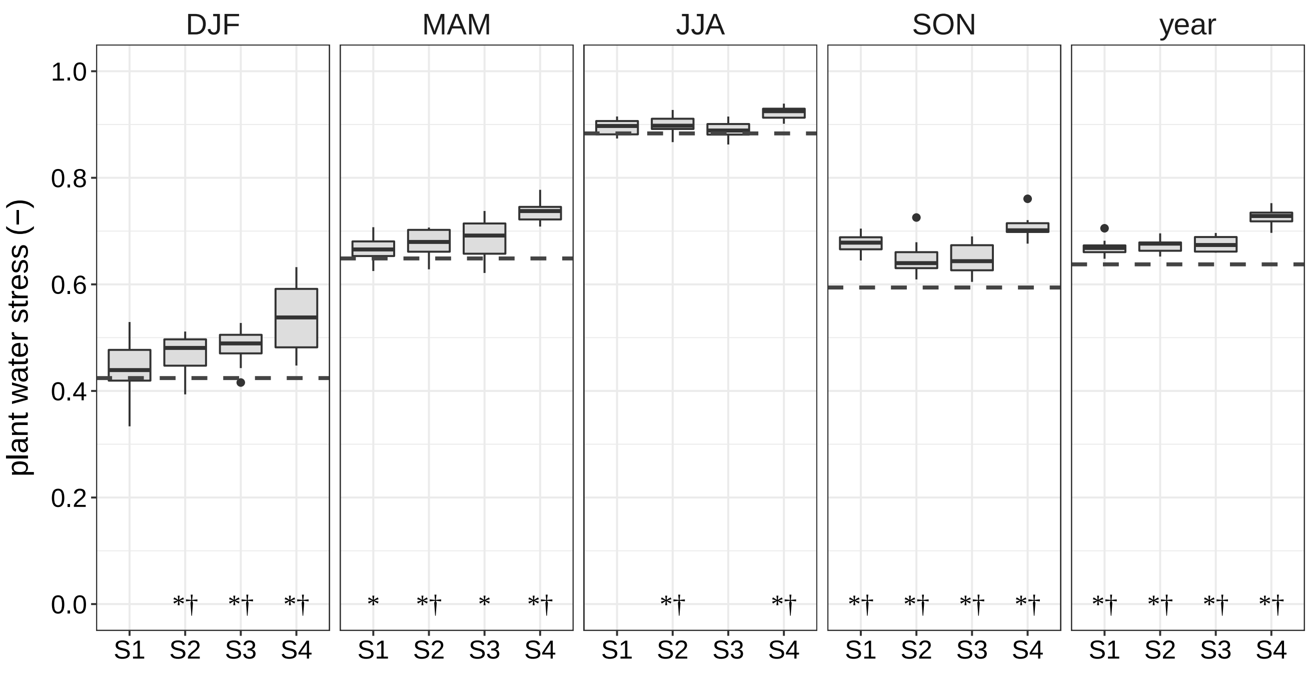

Figure S6. Catchment-average plant water stress (-), averaged by season: winter (DJF), spring (MAM), summer (JJA), autumn (SON), and for the whole year. The boxplots indicate the spread of the catchment-average among the nine climate models. In each panel the horizontal dashed line represents the catchment-average value for the reference scenario. An asterisk (∗) indicates a robust change and a dagger (†) indicates a significant change ($p<0.05$).

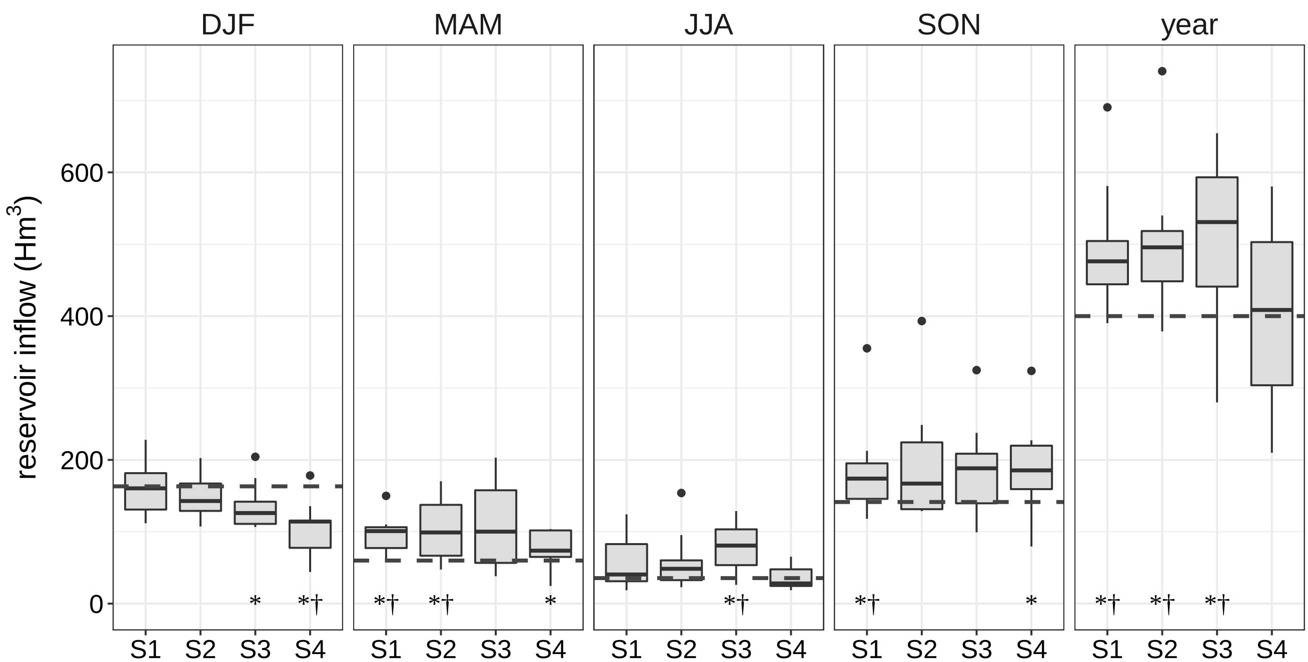

Figure S7. Catchment-average reservoir inflow (Hm^3), averaged by season: winter (DJF), spring (MAM), summer (JJA), autumn (SON), and for the whole year. The boxplots indicate the spread of the catchment-average among the nine climate models. In each panel the horizontal dashed line represents the catchment-average value for the reference scenario. An asterisk ($*$) indicates a robust change and a dagger (†) indicates a significant change ($p<0.05$).

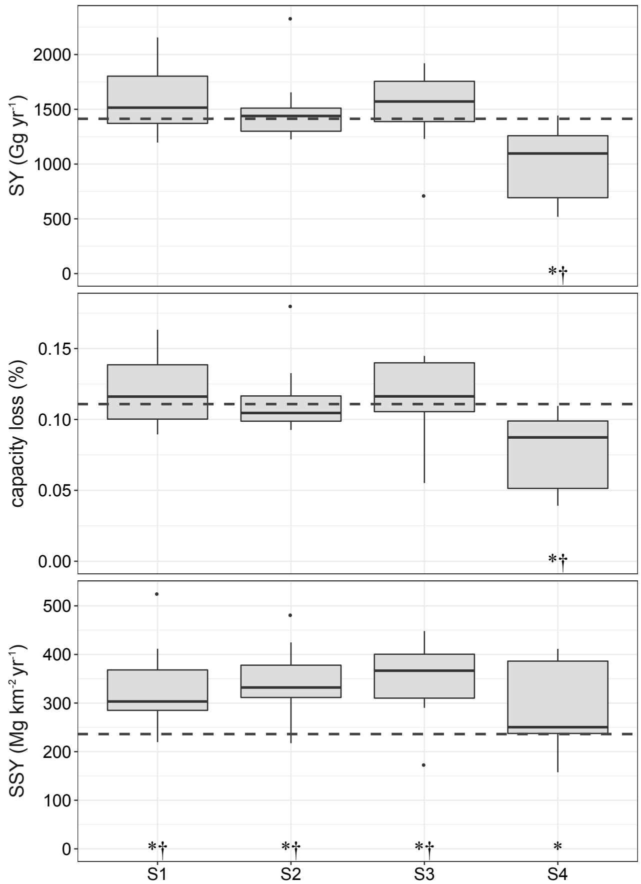

Figure S8. Catchment-average reservoir sediment yield (SY) ($\mathrm{Gg\,yr^{-1}}$), capacity loss (%) and hillslope erosion (SSY) ($\mathrm{Mg\,km^{-2}\,yr^{-1}}$). The boxplots indicate the spread of the catchment-average among the nine climate models. In each panel the horizontal dashed line represents the catchment-average value for the reference scenario. An asterisk ($*$) indicates a robust change and a dagger (†) indicates a significant change ($p<0.05$).

Table S1. The name and capacity of the 14 reservoirs considered in this study. The reservoir number corresponds to the numbers in Figure 1b.

nr	name	capacity (Hm^3)
1	Taibilla	9
2	Fuensanta	210
3	Talave	35
4	Cenajo	437
5	Camarillas	36
6	Argos	10
7	Alfonso XIII	22
8	La Cierva	7
9	Valdeinfierno	13
10	Puentes	26
11	Algeciras	45
12	Ojós	1
13	Mayes	2
14	Crevillente	13

Table S2. The nine climate models used in this study, with their corresponding RCM, GCM and research institute.

RCM GCM	CCLM[a]	HIRHAM5[b]	RACMO[c]	RCA[d]	WRF[e]
CNRM-CM5	X			X	
EC-EARTH	X	X	X	X	
IPSL-CM5A-MR					X
MPI-ESM-LR	X			X	

[a]Climate Limited-area Modelling-Community (CLMcom), [b]Danish Meteorological Institute (DMI), [c]Royal Netherlands Meteorological Institute (KNMI), [d]Swedish Meteorological and Hydrological Institute (SMHI), [e]Institut Pierre Simon Laplace (IPSL)